Hurricane Predictability Analysis with Singular Vectors in the Multiresolution Global Shallow Water Model

XIAOXU TIAN[a] AND KAYO IDE[a]

[a] *Department of Atmospheric and Oceanic Science, University of Maryland, College Park, College Park, Maryland*

(Manuscript received 6 August 2020, in final form 24 January 2021)

ABSTRACT: In this study, the tangent linear and adjoint (TL/AD) models for the Model for Prediction Across Scales (MPAS) Shallow Water (SW) component are tested and demonstrated. Necessary verification check procedures of TL/AD are included to ensure that the models generate correct results. The TL/AD models are applied to calculate the singular vectors (SVs) with a 48-h optimization time interval (OTI) under both the quasi-uniform-resolution (UR) and smoothly variable-resolution (VR) meshes in the cases of Hurricanes Sandy (2012) and Joaquin (2015). For the global domain, the VR mesh with 30 210 grid cells uses slightly fewer computational resources than the UR mesh with 40 962 cells. It is found that at the points before Hurricanes Sandy and Joaquin made sharp turns, the leading SV from the VR experiment show sensitivities in both areas surrounding the hurricane and those relatively far away, indicating the significant impacts from the environmental flows. The leading SVs from the UR experiments are sensitive to only areas near the storm. Forecasts by the nonlinear SW model demonstrate that in the VR experiment, Hurricane Sandy has a northwest turn similar to the case in the real world while the storm gradually disappeared in the UR experiment. In the case of Hurricane Joaquin, the nonlinear forecast with the VR mesh can generate a track similar to the best track, while the storm became falsely dissipated in the forecast with the UR mesh. These experiments demonstrate, in the context of SW dynamics with a single layer and no physics, the track forecasts in the cases of Hurricanes Sandy and Joaquin with the VR mesh are more realistic than the UR mesh. The SV analyses shed light on the key features that can have significant impacts on the forecast performances.

KEYWORDS: Atmosphere; Shallow-water equations; Hurricanes/typhoons; Mesoscale processes; Singular vectors; Numerical weather prediction/forecasting

1. Introduction

One of the challenges in numerical weather prediction (NWP) has been to resolve atmospheric motions at scales as fine as possible, which is especially the case for global models. Even with the computational capabilities developed so far, global atmospheric simulations at the convective scales require an enormous amount of resources (Yeh et al. 2002; Satoh et al. 2008). The Model for Prediction Across Scales (MPAS) simulation framework developed by the National Center for Atmospheric Research (NCAR) offers the options of global simulation with both uniform and smoothly variable resolutions (Ringler et al. 2008; Skamarock et al. 2012; Park et al. 2013). A prominent feature of MPAS is that the model employs finite-volume irregular spherical centroidal Voronoi tessellations (SCVT) meshes on a C grid (Thuburn et al. 2009). The SCVT mesh allows, in addition to uniform resolution throughout the globe, enhanced resolutions over a chosen region and coarse resolutions at the rest of the global domain with gradual and smooth transitions in between. Thus, no abrupt changes in resolutions will exist as in the Weather Research and Forecasting (WRF) Model's nesting configuration. Hagos et al. (2013) found that the errors generated near the edges of the high-resolution nesting regions in WRF simulations are no longer present in the results from MPAS using smoothly variable-resolution mesh. Rauscher and Ringler (2014) demonstrated that the variable-resolution mesh improves the ability of the model dynamics in resolving transient eddies activities. MPAS was made available to the public by NCAR (Michaelis et al. 2019).

Lorenz (1975) pointed out that forecast uncertainties, in general, come from the errors in the initial conditions (ICs) and the errors in the forecast model. With a given forecast model, the predictability of weather and climate can be investigated by calculating the optimal excitation of perturbations, i.e., the singular vector (SV) method (Lorenz 1965; Farrell 1989). In the pioneering work of Lorenz (1965), it is pointed out that the fastest-growing perturbations for a given period of model simulations can be obtained by calculating the singular vectors of the linearized version of the nonlinear forecast model, which is also called a tangent linear model. The tangent linear model and its transpose, also called the adjoint model, are required for calculating the SVs. This SV approach was later adopted by numerous studies to effectively determine atmospheric model features, including flow-dependent predictabilities, atmospheric instabilities, and weather forecast errors (Lacarra and Talagrand 1988; Farrell 1989; Borges and Hartmann 1992). At the European Centre for Medium-Range Weather Forecasts (ECMWF), Buizza (1994), Palmer et al. (1944), and Buizza and Palmer (1995) calculated the singular vectors of the operational global forecast model and found that its predictabilities are highly dependent on the background flow features. Mureau et al. (1993) and Molteni et al. (1996) initialized the ensemble of perturbations with the leading SVs for forecasts with the ECMWF model.

In exploring the predictability of the smoothly variable-resolution mesh by the MPAS model, the dynamic solver of

Corresponding author: Xiaoxu Tian, xtian15@terpmail.umd.edu

DOI: 10.1175/JAS-D-20-0238.1

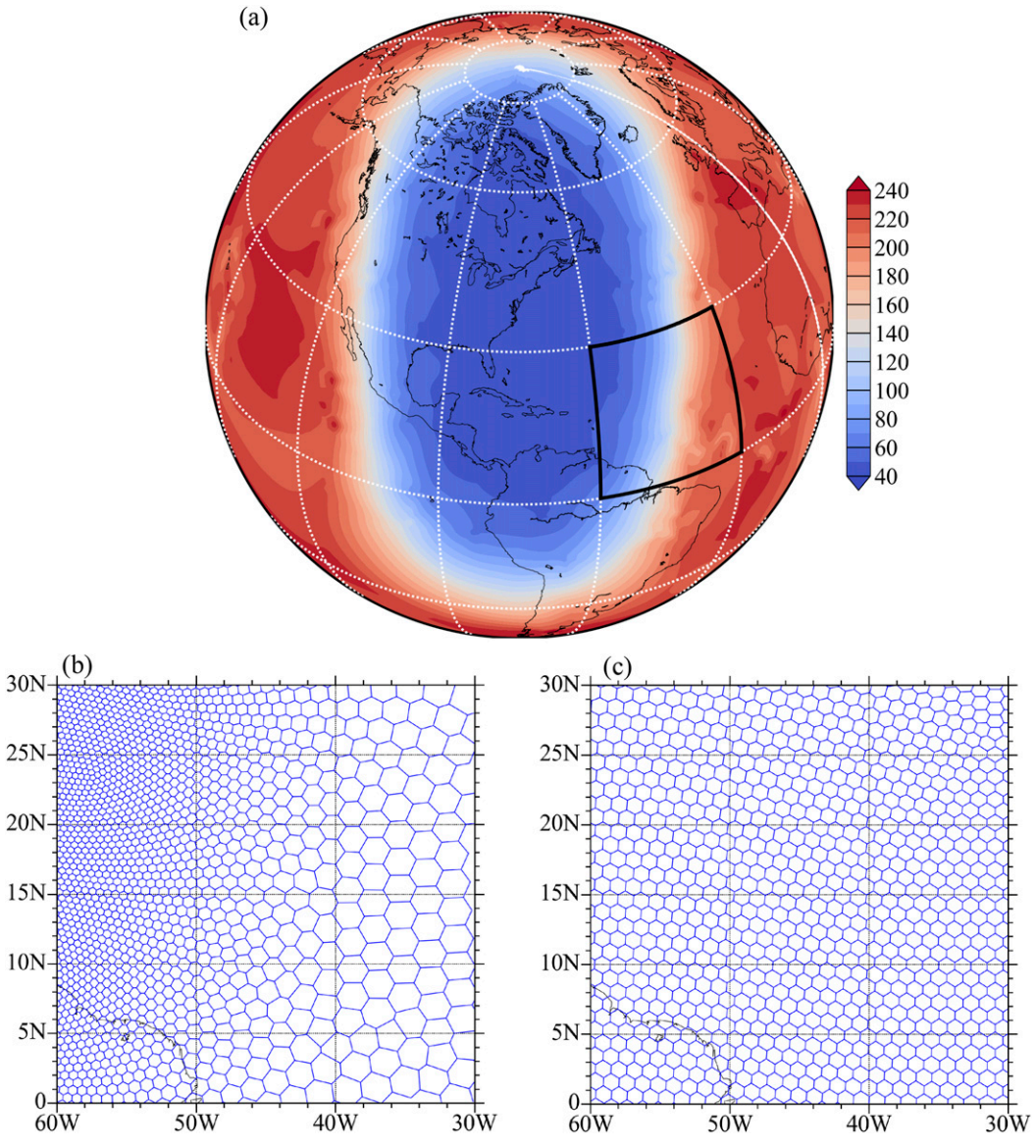

FIG. 1. (a) Distances between neighboring grid cells in the variable-resolution mesh that has 30 210 cells to cover the entire global area. The center of the area with refined resolution is at (35°N, 75°W]). (b) The variable-resolution centroidal Voronoi mesh distribution inside the black box defined in (a). (c) As in (b), but with the quasi-uniform-resolution mesh that has 40 962 grid cells globally.

shallow water (SW) equations is adopted in this study. Despite the availability of sophisticated atmospheric models like MPAS-Atmosphere, simple dynamical models such as MPAS-SW remain broadly feasible tools in realistically simulating some behaviors of the atmosphere. The shallow water equations permit a close representation of the atmospheric dynamics, which allows the matching of wind and potential vorticity to some extent (Juckes 1989). The SW model captures interactions between waves and vortical motions in rotating fluids with inexpensive computational costs (Kent et al. 2017). The SW model, combined with the barotropic model, was implemented operationally for hurricane track forecasts (Demaria et al. 1992). The SW equations under the global MPAS framework was first described in Ringler et al. (2008) to apply the multiresolution SCVT mesh into global numerical modeling and was further validated in Ringler et al. (2010) with a set of standard test cases for its robustness.

Based on the nonlinear MPAS-SW model, in this study, the corresponding tangent linear (TL) and adjoint (AD) models are first developed manually line by line following the detailed guidance in Zou et al. (1997) and Tian and Zou (2020). In addition to the essential role in obtaining model singular vectors, the TL/AD models also have versatile applicabilities,

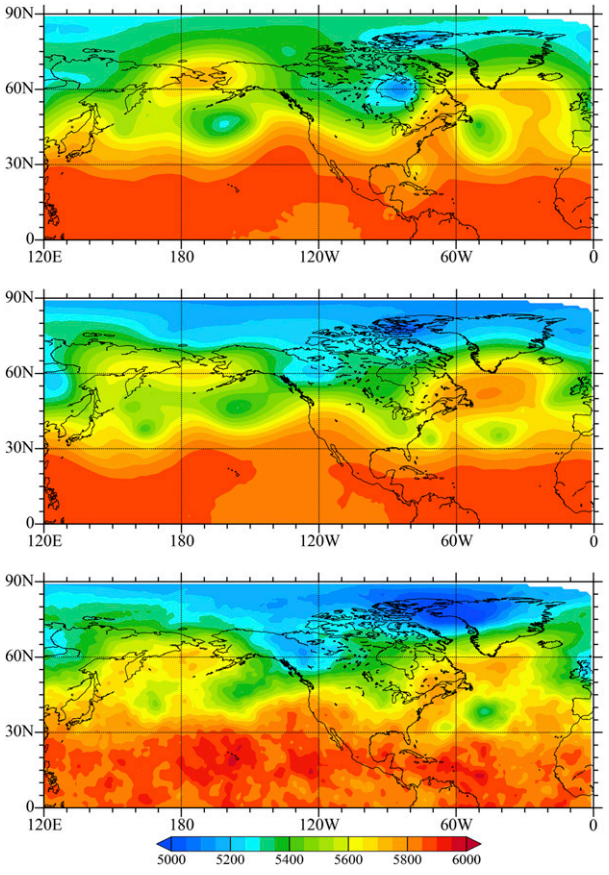

FIG. 2. Geopotential heights at 500 hPa at 0000 UTC (a) 27 and (b) 29 Oct 2012 from ERA5. (c) The 48-h MPAS-SW forecast of geopotential heights at 500 hPa valid at 0000 UTC 29 Oct 2012 taking (a) as the initial conditions.

including sensitivity analyses and variational data assimilation (Zou et al. 1997; Errico and Vukicevic 1992; Errico 1997). In Errico and Vukicevic (1992), the adjoint model of the Pennsylvania State University (PSU)–NCAR mesoscale model (MM4) was applied to efficiently and accurately calculate the sensitivities of a chosen scalar quantity of interest at a forecast time to the model ICs. Tian and Zou (2020) documented the development of TL/AD of the global MPAS-Atmosphere model and demonstrated the applicability of the MPAS-Atmosphere adjoint model in efficiently obtaining sensitivities of a response function at forecast time to the ICs in a baroclinic wave case. In this study, the TL/AD models of MPAS-SW are applied to calculate the singular vectors under both uniform and smoothly variable resolutions to investigate the predictability in the context of SW dynamics. In section 2, more details of the nonlinear MPAS-SW model are introduced. The TL/AD models' developments are described in section 3 and the singular vectors' calculations in section 4. The SV results in Hurricanes Sandy (2012) and Joaquin (2015) from the experiments under both the uniform- and variable-resolution meshes will be discussed in section 5. Section 6 summarizes and concludes this research.

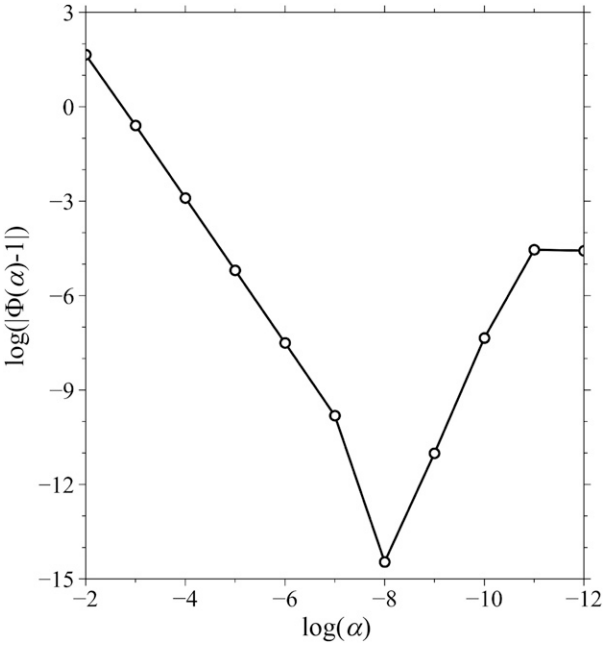

FIG. 3. Variations of the function $\log(|\Phi(\alpha) - 1|)$ for the correctness check of the MPAS-SW tangent linear model for the 24-h forecast with respect to the initial perturbation scaling factor α.

2. MPAS-SW model description

The shallow water equations have been widely applied in analyzing the dynamics of rotating and stratified fluids in meteorology and oceanography. The MPAS-SW model makes forecasts following the SW equations discretized to the irregular hexagonal Voronoi grids. The nonlinear SW equations may be written as follows (Ringler et al.2010):

$$\frac{\partial h}{\partial t} + \nabla(h\mathbf{u}) = 0, \tag{1}$$

$$\frac{\partial \mathbf{u}}{\partial t} + (\mathbf{u}\nabla)\mathbf{u} + f\,\mathbf{k}\times\mathbf{u} = -g\nabla(h+b), \tag{2}$$

where the model prognostic variables are the fluid thicknesses h and the velocity vectors $\mathbf{u}$. The Coriolis parameter, $f = 2\Omega\sin\varphi$, varies with the latitude φ throughout the globe, in which the Ω is the rotation rate of Earth. The quantity b in Eq. (2) denotes bottom topography height, which is set as zeros everywhere in the experiments of this study. The model is spatially discretized following the Arakawa C grid (Thuburn et al. 2009). Thus, the variable h is located at the cell centers, while the velocity vectors $\mathbf{u}$ are at the edges of each cell with directions normal to the edges. Figure 1 is an example showing the meshes of both smoothly variable resolution (VR) and quasi-uniform resolution (UR). Figures 1a and 1b illustrate the cell distances and actual spatial distribution of the cells in the VR mesh that has in total of 30210 cells globally. The resolutions range from 48 to 240 km. The center of the area with refined resolution (blue shadings) is located at 35°N, 75°W in order to entirely cover the periphery regions that Hurricanes Sandy and Joaquin pass by, which will be discussed in-depth in

TABLE 1. Correctness check results of the MPAS-SW adjoint model when it is integrated for 1, 6, 12, 18, and 24 h; lhs: left-hand side; rhs: right-hand side.

Time (h)	lhs	rhs	(lhs − rhs)/lhs
1	328 400.508 977 852 2	328 400.508 977 852 2	0.0
6	330 562.873 921 961 3	330 562.873 921 961 4	$3.521\,730\,085\,587\,831 \times 10^{-16}$
12	336 961.913 417 705 04	336 961.913 417 705 04	0.0
18	347 456.022 655 873 8	347 456.022 655 873 8	0.0
24	362 645.085 624 939 65	362 645.085 624 939 6	$1.605\,086\,163\,325\,754\,4 \times 10^{-16}$

later sections. However, this center location and the orientation of the high-resolution area can be relocated and pivoted depending on any other studies' needs. Compared with the VR, the resolution of the UR mesh is about 120 km uniformly throughout the globe, which has in total of 40 962 cells. In addition, a uniform 30-km high-resolution (HR) mesh consisting of 655 362 cells is also included, the simulation results from which are referenced by those from both VR and UR. Temporally, the fourth-order Runge–Kutta integral scheme was adopted to achieve the fourth-order accuracy in time (Ringler et al. 2008). In addition to the prognostic variables h and $\mathbf{u}$, diagnostic variables including wind vectors tangential to cell edges v, traditional zonal u_λ and meridional u_φ wind vectors, divergences $\nabla\mathbf{u}$, and vorticities $\nabla \times \mathbf{u}$ are also calculated within each time integration step.

The ICs for MPAS-SW to start simulations are obtained from the ERA5 dataset from the ECMWF, specifically at 500 hPa with the resolution of 0.25° × 0.25°. As midtropospheric flows are nearly nondivergent, short-term forecasts of flows at this level can be simulated with simple models like SW (Holton 1973). The geopotential heights (zonal and meridional winds) at 500 hPa are first interpolated to the geographical locations of the cell centers (cell edges). The conventional zonal and meridional wind vectors are transformed into those that are normal to cell edges following the relationship of

$$u_{\text{mpas}} = u_\lambda \cos\theta + u_\varphi \sin\theta, \tag{3}$$

where u_{mpas} denotes an element in the prognostic variables $\mathbf{u}$ in Eq. (2), i.e., the wind vector normal to cell edges. The u_λ and u_φ represents zonal and meridional wind components, respectively. The θ is the angle between the edge's normal direction and the local eastward direction. Figure 2a gives the geopotential heights at 500 hPa at 0000 UTC 27 October 2012, which also serves as the IC of a 48-h forecast with the nonlinear MPAS-SW. Figures 2b and 2c are the geopotential heights at 48 h after Fig. 2a, which is 0000 UTC 29 October from the ERA5 (Fig. 2b) and MPAS-SW forecast (Fig. 2c). It can be seen that the geopotentials in the 48-h forecast made with MPAS-SW generally agrees with ERA5, especially the wave patterns near the 30°N and 60°N latitudes. Thus, to some extent, the SW equations can validly simulate the behaviors in the real atmosphere, as discussed in (Holton 1973).

3. Development of MPAS-SW TL/AD models

a. The tangent linear model

The nonlinear MPAS-SW model can be symbolically written as

$$\mathbf{x}(t_r) = \mathcal{M}[\mathbf{x}(t_0)], \tag{4}$$

where t_0 is the initial time and t_r a forecast time; $\mathbf{x}$ denotes the vector of prognostic variables including both h and $\mathbf{u}$; and $\mathcal{M}$ is the nonlinear MPAS-SW forward operator taking the IC $\mathbf{x}(t_0)$ as input and generating the forecast $\mathbf{x}(t_r)$ as output. The tangent linear model can be derived by linearizing $\mathcal{M}$ with respect to every prognostic and diagnostic variable, which can be written as

$$\Delta\mathbf{x}(t_r) = \mathbf{M}[\mathbf{x}(t_0)]\Delta\mathbf{x}(t_0) = \frac{\partial\mathcal{M}[\mathbf{x}(t_0)]}{\partial\mathbf{x}}\Delta\mathbf{x}(t_0). \tag{5}$$

In the equation above, the prefix Δ represents perturbations of the prognostic variables $\mathbf{x}$, and $\mathbf{M}$ is called the tangent linear operator of MPAS-SW. The TL model $\mathbf{M}$ takes small perturbations $\Delta\mathbf{x}(t_0)$ as ICs, propagates these perturbations following the background fluid trajectory, and predicts the distributions of the perturbations at the forecast time t_r. As the TL model is obtained by linearizing the nonlinear MPAS-SW model, the smaller the magnitudes of the perturbations are, the more accurately the TL model can predict the perturbation evolutions. Similarly, the correctness of the developed MPAS-SW TL model may be verified following the relationship as

$$\Phi(\alpha) = \frac{\|\mathcal{M}(\mathbf{x}+\alpha\mathbf{p}) - \mathcal{M}(\mathbf{x})\|}{\|\mathbf{M}(\mathbf{x})\alpha\mathbf{p}\|} = 1 + O(\alpha). \tag{6}$$

In this equation, α is a scaling factor that controls the magnitudes of the nonzero perturbation vector $\mathbf{p}$. As α becomes smaller and smaller, the predicted perturbations by the MPAS-SW TL model, $\mathbf{M}(\mathbf{x})\alpha\mathbf{p}$, should be expected to be increasingly closer to the differences between the nonlinear forecast results with and without perturbations in the ICs, i.e., $\mathcal{M}[\mathbf{x}(t_0)+\alpha\mathbf{p}] - \mathcal{M}[\mathbf{x}(t_0)]$. The numeric results for correctness verification of the MPAS-SW TL is given in Fig. 3. Both the x and y axis use a logarithm scale.

TABLE 2. Computation time in seconds of 24-h simulations with a single core by the nonlinear forward (FWD), tangent linear, and adjoint models under UR (40 962 cells) and VR (30 210 cells) meshes both with a 180-s time step.

Model	Time (s)	
	UR	VR
FWD	71	50
TL	120	85
AD	230	160

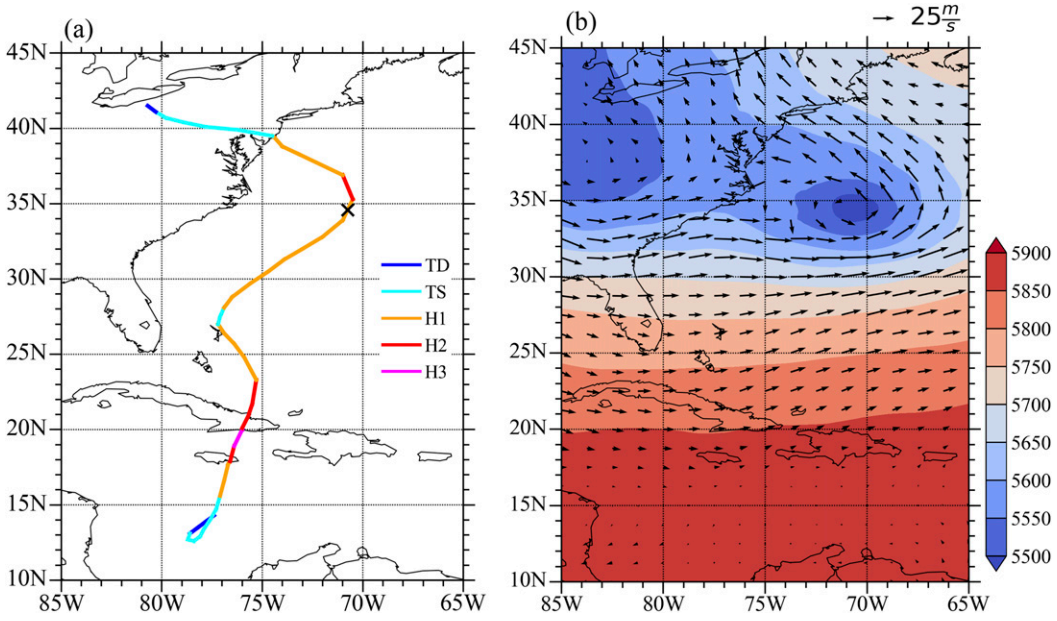

FIG. 4. (a) The track of Hurricane Sandy from 21 to 31 Oct 2012 from best track records. The colors of the curve represent the intensity of the hurricane following the Saffir–Simpson scale. The black cross marks the location of Hurricane Sandy at 0300 UTC 29 Oct 2012. (b) The fields of height and wind vectors at 500 hPa at 0300 UTC 29 Oct 2012.

As the scaling factor α approaches zero in the x axis, the quantity $\Phi(\alpha)$ in Eq. (6) gradually approaches unity until α becomes smaller than 10^{-8}, at which time the machine round-off errors start to affect the calculation results.

b. The adjoint model

The adjoint model $\mathbf{M}^{\mathrm{T}}$ is essentially the transpose of the tangent linear model $\mathbf{M}$, which can be symbolically expressed as

$$\Delta\hat{\mathbf{x}}(t_0) = \mathbf{M}^{\mathrm{T}}(\mathbf{x})\Delta\hat{\mathbf{x}}(t_r); \tag{7}$$

$\Delta\hat{\mathbf{x}}$ is the adjoint variable, t_r the final time of the forecast period. It is to be noted that the adjoint model takes the adjoint variable at the final time t_r, integrates backward in time, and generates the output at the starting time t_0 of the simulation period. As the adjoint model runs backward in time, the nonlinear forward simulations' flow trajectory is still required in the adjoint calculation processes. Thus, in the system developed in this research, it was decided that the prognostic variables h and $\mathbf{u}$ will be stored at every time step of the simulation period, while the diagnostic variables are updated by recalculation within each step. As the adjoint model is fundamentally the transpose of the tangent linear model, for any two vectors $\Delta\mathbf{x}_1$ and $\Delta\mathbf{x}_2$, the following relationship should be satisfied:

$$\langle\Delta\mathbf{x}_2, \mathbf{M}\Delta\mathbf{x}_1\rangle = \langle\mathbf{M}^{\mathrm{T}}\Delta\mathbf{x}_2, \Delta\mathbf{x}_1\rangle. \tag{8}$$

The left-hand side (lhs) is the inner product of $\Delta\mathbf{x}_2$ and the tangent linear model taking $\Delta\mathbf{x}_1$ as initial perturbations and integrating from time t_0 to t_r. The right-hand side (rhs), on the other hand, is the inner product of the output from the adjoint model taking $\Delta\mathbf{x}_2$ as the adjoint initial conditions and integrating backward from time t_r to t_0 and the vector $\Delta\mathbf{x}_1$. If the adjoint model is developed correctly, the lhs and rhs should match to the machine accuracy. In MPAS-SW, every variable is declared as double-precision types, the accuracy of 10^{-13} or better is expected for the results of Eq. (8). For integration durations from 1 to 24 h, the results following Eq. (8) are given in Table 1. In all of the test cases, the lhs and rhs agree with each other either completely or to the precision of 10^{-16}, indicating the correctness of the developed MPAS-SW adjoint model. Similar to Tian and Zou (2020) studied, the MPAS-SW adjoint model can readily be applied to efficiently obtain the sensitivity field in a quantity of interest at the forecast time to the ICs. As introduced in section 2, the VR (UR) mesh consists of 30210 (40962) cells. With the same 180-s time step, the actual time (in seconds) spent to run the nonlinear forward, TL, and AD MPAS-SW model for a 24-h simulation with a single core of a desktop is given in Table 2. It confirms that the number of cells in a mesh is a direct indicator of the computation cost.

4. Singular vectors of the MPAS-SW TL model

The matrix of an atmospheric model is often of dimensions that are not computationally tractable. Thus, in studies such as Buizza (1994) and Farrell and Moore (1992), the singular vectors are obtained through iterative methods such as the power method and Lanczos algorithm (Strang and Freund 1986) that allow the matrices to be implicitly accounted for. Farrell and Moore (1992) found the leading singular vector of a quasigeostrophic model by iteratively running its TL and AD models. In comparison, Buizza (1994) adopted the Lanczos

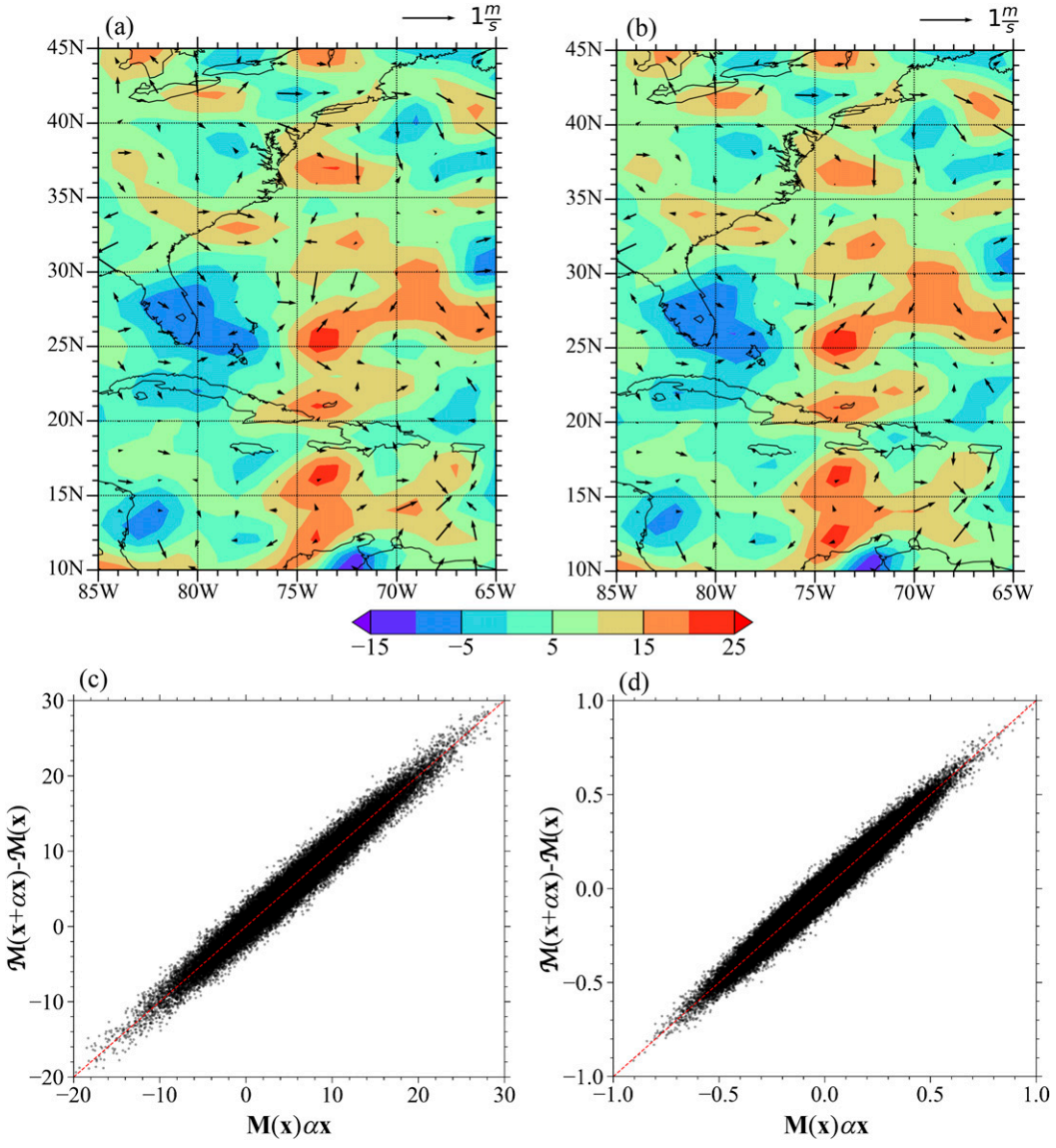

FIG. 5. (a) The differences in h (shaded) and $\mathbf{u}$ (vectors) of 4-day nonlinear model simulations under UR mesh between the perturbed and unperturbed $\mathcal{M}(\mathbf{x} + \alpha\mathbf{x}) - \mathcal{M}(\mathbf{x})$ and (b) the 4-day tangent linear model simulations with the same perturbation added upon to initial conditions $[\mathbf{M}(\mathbf{x})\alpha\mathbf{x}]$ in (a). (c),(d) Scatterplots of $\mathcal{M}(\mathbf{x} + \alpha\mathbf{x}) - \mathcal{M}(\mathbf{x})$ and $\mathbf{M}(\mathbf{x})\alpha\mathbf{x}$ for the state variable (c) h and (d) $\mathbf{u}$ with results from the entire global region included. The correction coefficients for the $\mathcal{M}(\mathbf{x} + \alpha\mathbf{x}) - \mathcal{M}(\mathbf{x})$ and $\mathbf{M}(\mathbf{x})\alpha\mathbf{x}$ in (c) and (d) are 0.981 and 0.982.

algorithm that allows more than one SVs of the ECMWF operational model to be found, results of which are orthogonal to each other to the machine accuracy conforming to the theoretical basis. In this study, the Lanczos algorithm is adopted to find the MPAS-SW TL model's leading SVs. A norm is first defined as

$$\|\Delta\mathbf{x}(t_r)\|_E^2 = \langle \Delta\mathbf{x}(t_r), \Delta\mathbf{x}(t_r)\rangle. \tag{9}$$

Substituting Eqs. (5) and (8) into (9), where the perturbation at t_r can be obtained through the MPAS-SW TL model $\mathbf{M}$, the norm can be rewritten as

$$\|\Delta\mathbf{x}(t_r)\|_E^2 = \langle \mathbf{M}\Delta\mathbf{x}(t_0), \mathbf{M}\Delta\mathbf{x}(t_0)\rangle = \langle \mathbf{M}^{\mathrm{T}_\mathbf{E}}\mathbf{M}\Delta\mathbf{x}(t_0), \mathbf{x}(t_0)\rangle, \tag{10}$$

in which the $\mathbf{M}^{\mathrm{T}_\mathbf{E}} = \mathbf{E}^{-1}\mathbf{M}^{\mathrm{T}}\mathbf{E}$ and $\mathbf{E}$ is a diagonal coefficient matrix in the definition of the norm that will also be explained later. The perturbation that maximizes the norm defined as $||\mathbf{x}(t_r)||^2$ is then the eigenvector of the self-adjoint or Hermitian operator $\mathbf{M}^{\mathrm{T}_\mathbf{E}}\mathbf{M}$ associated with the greatest eigenvalue (Buizza 1994),

$$(\mathbf{M}^{\mathrm{T}_\mathbf{E}}\mathbf{M})\boldsymbol{\nu}_i(t_0) = \sigma_i^2\boldsymbol{\nu}_i(t_0), \tag{11}$$

in which the solved $\boldsymbol{\nu}_i$ are the eigenvectors of the matrix $\mathbf{M}^{\mathrm{T}_\mathbf{E}}\mathbf{M}$ or the singular vectors of the TL model $\mathbf{M}$. As $\mathbf{M}^{\mathrm{T}_\mathbf{E}}\mathbf{M}$ is self-adjoint,

TABLE 3. Singular values of the five leading singular vectors in both UR and VR experiments.

	UR		VR		HR	
i	σ_i^2	Percentage	σ_i^2	Percentage	σ_i^2	Percentage
1	6541.86	93.13%	2103.94	52.21%	851.11	48.12%
2	225.42	3.21%	799.32	19.83%	399.22	22.57%
3	115.27	1.64%	501.96	12.46%	275.63	15.58%
4	74.51	1.06%	349.05	8.66%	130.76	7.39%
5	67.62	0.96%	275.65	6.84%	111.87	6.33%

the singular values σ_i are real and the SVs $\boldsymbol{\nu}_i$ form a complete and orthogonal set at the time t_0 (Zou et al. 1997).

In this study, the norm is specifically defined as the total perturbation energy (TPE) $\mathcal{E}$ of the MPAS-SW model,

$$\mathcal{E} = \frac{1}{2A}\int (H\Delta\mathbf{u}^2 + g\Delta h^2)\, dA, \tag{12}$$

where H is the mean height, and $1/A$ denotes an average over the global domain. Letting $\Delta\mathbf{x}$ represent the perturbation vector, the norm of TPE can also be written as

$$\mathcal{E} = \langle \Delta\mathbf{x}, \mathbf{E}\Delta\mathbf{x}\rangle, \tag{13}$$

where $\mathbf{E}$ again is a diagonal matrix of the TPE coefficients. In the case of Eq. (12), the matrix $\mathbf{E}$ = diag$\{(1/2)H, (1/2)H, \ldots, (1/2)H, (1/2)g, (1/2)g, \ldots, (1/2)g\}$, in which the $(1/2)H$ spans the length of $\mathbf{u}$ and the $(1/2)g$ spans the length of h. To maintain the self-adjointness of $\mathbf{M}^{\mathrm{T}_\mathbf{E}}\mathbf{M}$ in the presence of $\mathbf{E}$, the eigenvalue problem in Eq. (11) may now be transformed into

$$(\mathbf{E}^{1/2}\mathbf{M}^{\mathrm{T}_\mathbf{E}}\mathbf{M}\mathbf{E}^{-1/2})\tilde{\boldsymbol{\nu}}_i = \mathbf{E}^{-1/2}\mathbf{M}^{\mathrm{T}}\mathbf{E}\mathbf{M}\mathbf{E}^{1/2}\tilde{\boldsymbol{\nu}}_i = \sigma_i^2\tilde{\boldsymbol{\nu}}_i. \tag{14}$$

The eigenvector obtained by solving Eq. (14): $\tilde{\boldsymbol{\nu}}_i = \mathbf{E}^{1/2}\boldsymbol{\nu}_i$. A subprogram following Eq. (14) can thus be utilized in the Lanczos algorithm to solve for the eigenvalues and eigenvectors.

5. SVs in case studies

a. Hurricane Sandy

Hurricane Sandy, as shown in Fig. 4a, appeared near the Caribbean Sea as a tropical depression, rapidly intensified into a category 3 hurricane, and made its landfall in Cuba (Tian and Zou 2016). The storm moved northwestward, weakened to a tropical storm before starting to regain its strength, and turned northeastward as a category 1 hurricane. At 0600 UTC 29 October, the storm underwent a dramatic northwest turn and headed toward the coast of New Jersey, the United States. The SVs under the UR and VR meshes shown in Fig. 1 are demonstrated with the case of Hurricane Sandy. Specifically, the time at 0300 UTC 29 October, 3 h before the storm's dramatic turn, was chosen as the initial time in both the UR and VR experiment with the MPAS-SW model. The geographical location of Hurricane Sandy at 0300 UTC 29 October was marked with a black cross in Fig. 4a, the wind and height fields at 500 hPa in Fig. 4b. To verify the closeness of the approximations by the TL model in propagating the perturbations, an initial perturbation of $\Delta\mathbf{x} = 10^{-3} \times \mathbf{x}$ was given to the MPAS-SW TL model and was integrated for four days. A simple scaling factor of 10^{-3} was chosen so that the magnitudes of the perturbations to both $\mathbf{u}$ and h are of the typical sizes of model errors for both variables (Tian 2021; Lindskog et al.2006). In the meantime, the nonlinear MPAS-SW model with and without the same perturbations were also run for the same length of time. Figure 5 shows the perturbations after four days obtained from the nonlinear model's differences with and without perturbations (Fig. 5a) and those from the TL model predictions (Fig. 5b). The patterns of the perturbations in both cases visually resemble each other quite closely. The scatterplots of h (Fig. 5c) and $\mathbf{u}$ (Fig. 5d) in the results are both closely aligned along the diagonal line with correlation coefficients of 0.981 and 0.982, respectively, indicating close approximations.

The first five SVs of the TL model with a 48-h optimization time interval (OTI) in the UR, VR, and HR experiments were calculated following the procedures in section 4 with the Lanczos algorithm. The singular values associated with the leading five SVs are given in Table 3. In UR, the norm accounted for by the first SV is more than 29 times of that by the second SV, while the ratios are not as significant in the cases of VR and HR. Both the h and $\mathbf{u}$ obtained in the first SV in VR, UR, and HR experiments are shown in Fig. 6. The sensitive regions in the first SV from the UR experiments are primarily near the center of Hurricane Sandy at the analysis time. In comparison, the results from the VR and HR experiments show sensitivities in both regions surrounding the hurricane center and areas that are far away, suggesting potential impacts from the environmental flows. It was pointed by Kim and Jung (2009) that, as the TC moves to the region of recurvature, the sensitivities of the leading SV to the environment flow become greater than those in nonrecurving scenarios. The results in Figs. 6b and 6c confirm the findings in Kim and Jung (2009). To verify the downstream impacts brought by the relatively ''isolated'' pattern northeast of 40°N, 40°W in Fig. 6b, perturbations on both h and $\mathbf{u}$ following only that pattern, as contoured in Fig. 7, are extracted. The nonlinear MPAS-SW model is then integrated for 48 h with and without the perturbations as contoured. Figures 7a and 7b are the evolved perturbations after 33 and 48 h calculated from differences between the nonlinear MPAS-SW model simulations. In the first 33 h, the pattern, starting from the

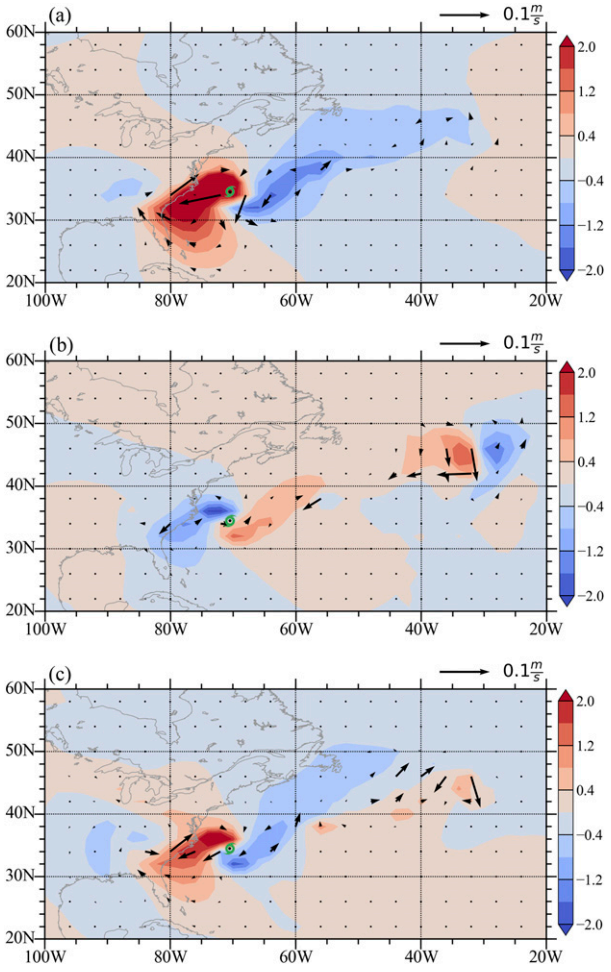

FIG. 6. The distributions of h (shaded) and $\mathbf{u}$ (vectors) in the leading singular vector with a 48-h optimization time interval from (a) UR, (b) VR, and (c) HR experiments.

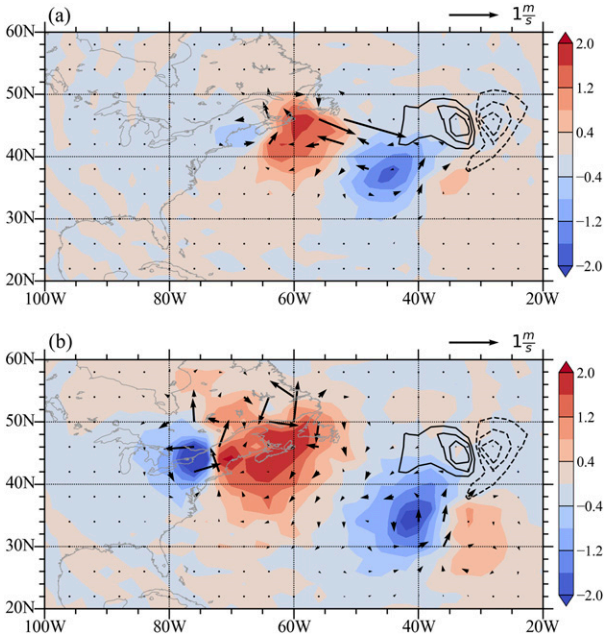

FIG. 7. Evolved perturbations after a (a) 33- and (b) 48-h forecast (shaded) when only the pattern on the east shown in Fig. 7a (contoured) is added to the initial conditions in the VR experiment.

east of 40°W, slowly propagated westward toward the coast. During the period between 33 and 48 h, the pattern was separated into two, one moved further toward the coast, and the other drifted south. The results confirm that the remotely isolated pattern to the northeast of Hurricane Sandy at the initial time will exert its influences within the 48-h OTI.

Forecasts are then made with the MPAS-SW model with the IC shown in Fig. 4b under the UR, VR, and HR meshes. It should be pointed out that SV results shown and discussed above are merely demonstrating how the optimal errors will evolve in forthgoing simulations. Nonetheless, the forecasts are made without any perturbations or SVs. The predicted storm evolutions with UR and VR are shown in Fig. 8, where the results from UR in the left column and those from VR in the right. Starting from 0300 UTC 29 October (Fig. 4b), a second low center appeared from the Arctic region that can be seen in the 9-h forecasts from both the UR and VR experiments (Figs. 8a,b). The coexistence triggered a Fujiwhara effect that caused the two systems to orbit each other counterclockwise, as shown in the 27-h forecast (Figs. 8c,d). However, the intensity of Hurricane Sandy in the UR results significantly weakened, while the polar cyclone strengthened as the dominant system. In contrast, in the VR experiment, Hurricane Sandy maintained its strength with respect to the polar cyclone. In the 33-h forecasts (Figs. 8e,f), the polar cyclone in the UR results still dominates Hurricane Sandy as Sandy moves further northeast, while in the VR experiment, the Fujiwhara effect carried on that drove Hurricane Sandy toward the coast of the United States. Hurricane Sandy nearly disappeared in the 45-h forecast of UR (Fig. 8g), but made its landfall in the forecast of VR (Fig. 8h). The nonlinear MPAS-SW forecast results under the HR mesh is given in Fig. 9. It can be found that the results from HR and VR agree with each other to a great extent in terms of the Fujiwhara effect and the sharp turn toward the U.S. coast. In both the VR and HR experiments, Hurricane Sandy maintained its dominant role with respect to the polar cyclone. Figure 10 is the track of Hurricane Sandy predicted using MPAS-SW under UR (solid curve), VR (dashed curve), and HR (dotted curve) meshes. Similar to what took place in the real world, Hurricane Sandy in the VR and HR experiments made a sharp northwest turn from its original northeast path, although with different landing points. In comparison, the predictions with the UR mesh was not able to simulate such behaviors.

To further investigate the underlying reasons for the significant differences in the patterns captured in the leading SVs, the nonlinear forecasts differences between the UR and HR and those between the VR and HR experiments at 0, 15, 24, and 30 h are shown in Fig. 11. Tian (2021) found that the errors

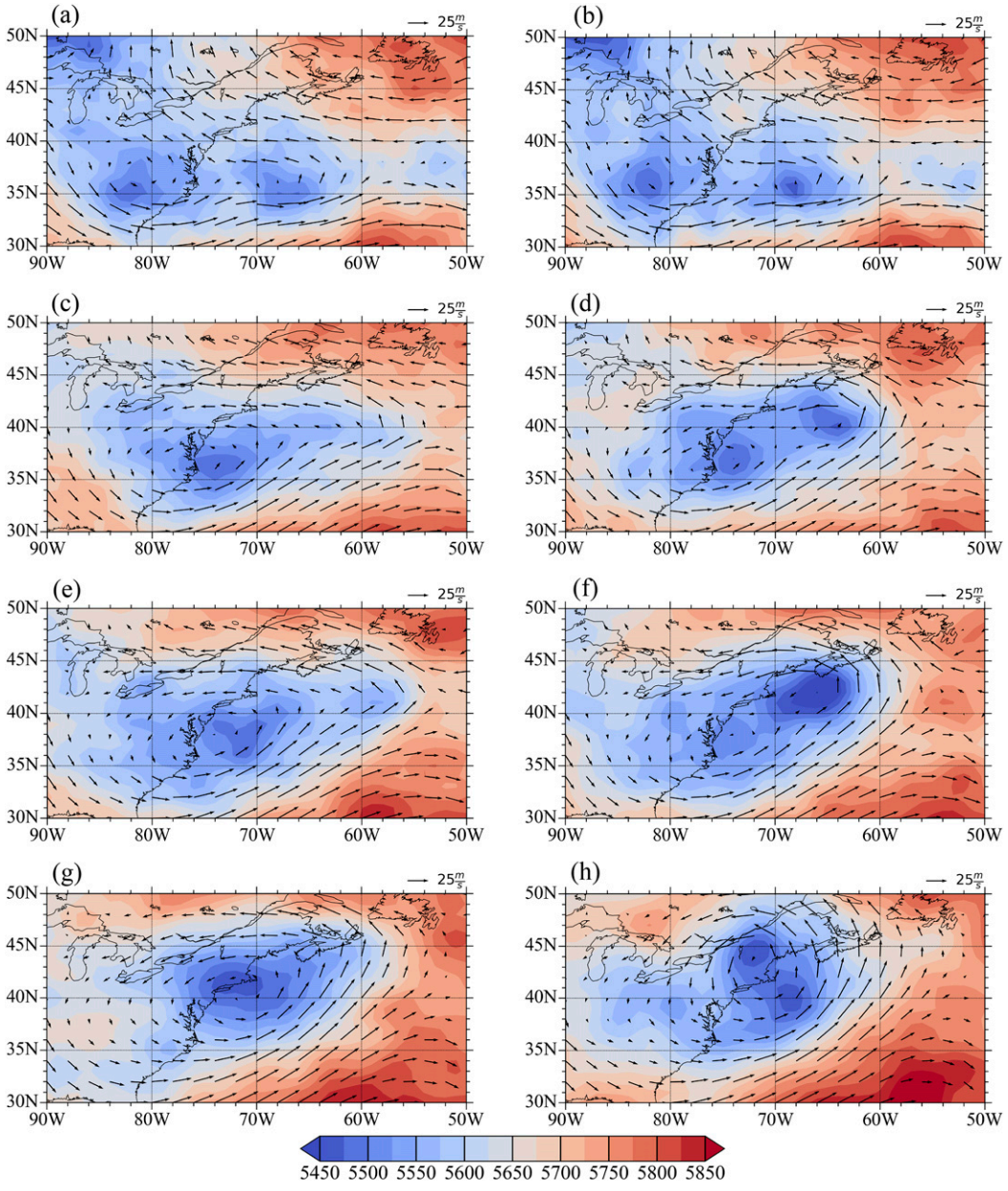

FIG. 8. Spatial distributions of the height (shaded) and wind vectors under (left) UR and (right) VR in the (a),(b) 9-, (c),(d) 27-, (e),(f) 33-, and (g),(h) 45-h forecasts starting from 0300 UTC 29 Oct 2012.

due to insufficient resolution, or undersampling errors, in the ICs will continuously increase with forecast time following weather signals simulated by the MPAS-SW model. In the case of VR, the simulations within the areas of fine resolutions will not contribute to aggravate the errors, as the dynamics within the areas are numerically solved under practically high resolutions. Figures 11a and 11b are the IC undersampling errors of UR and VR experiments compared to those of HR. In both cases, errors can be found both surrounding and to the northeast of Hurricane Sandy, just as identified by the VR SV shown in Fig. 6b. During the forecasts, the same as Fig. 7 revealed, the errors located far away from the hurricane kept propagating westward as the hurricane moves northeastward (Figs. 11c,d). The two systems encounter each other at about the time 24 h after the ICs (Figs. 11e,f). It is near the time of 24 h that the environmental factor made an impact on the hurricane track forecast. In Figs. 11g and 11h, the forecast differences between UR and HR (Fig. 11g) already display a significant storm dislocation, while the differences in VR and HR (Fig. 11h) show no such remarkable features. When focusing on the hurricane itself, the undersampling errors in the UR are always greater than those in VR due to the coarser resolutions. The structures

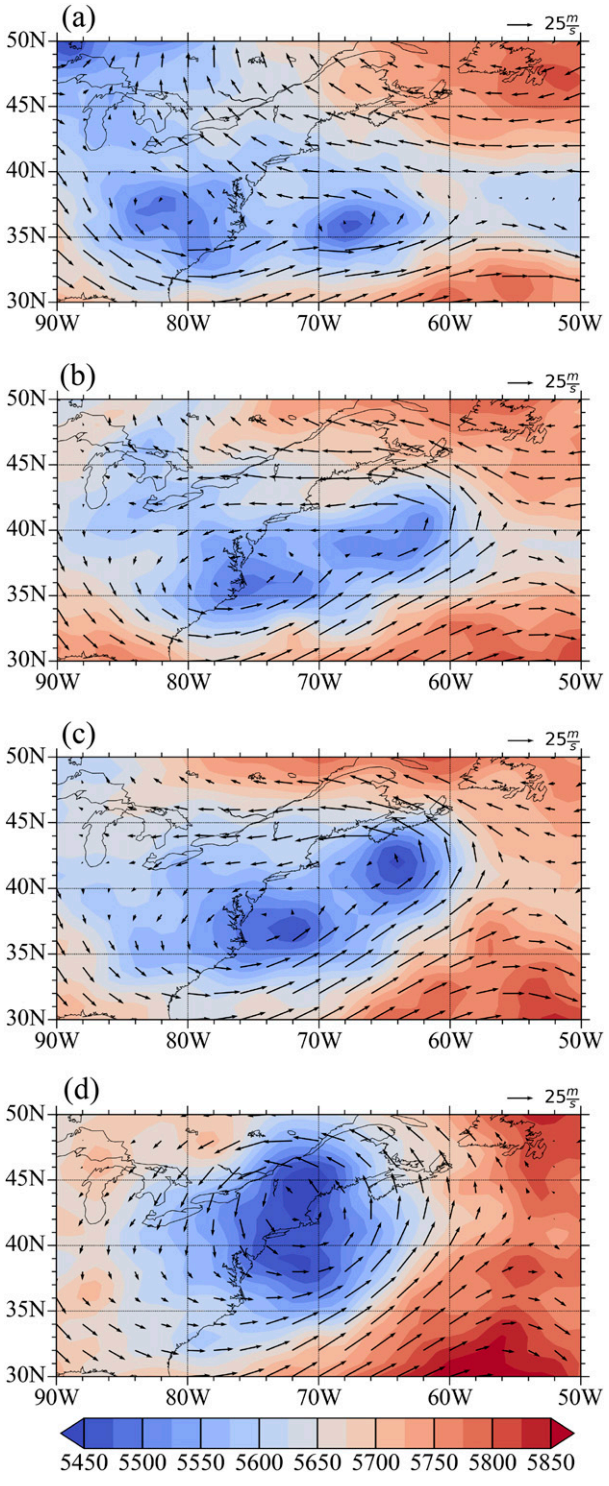

FIG. 9. Spatial distributions of the height (shaded) and wind vectors under HR in the (a) 9-, (b) 27-, (c) 33-, and (d) 45-h forecasts starting from 0300 UTC 29 Oct 2012.

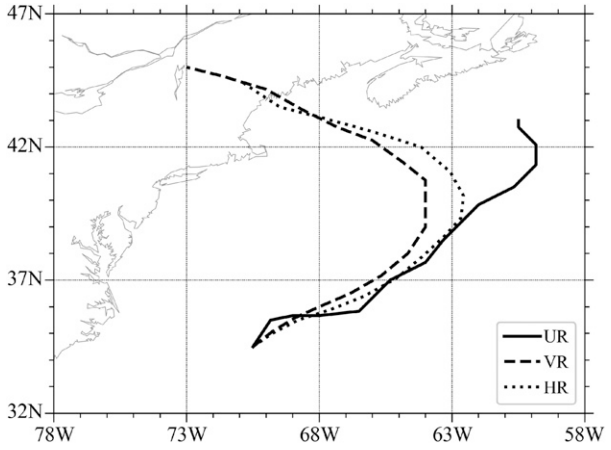

FIG. 10. The 48-h track forecast of Hurricane Sandy starting from 0300 UTC 29 Oct 2012 in the experiments with uniform-resolution (solid curve), variable-resolution (dashed curve), and high-resolution (dotted) meshes.

in the leading SVs and their associated norms that quantify TPE amplifications listed in Table 3 can then be combined with Fig. 11. In the UR experiment, the first SV accounts for the absolute majority (>93%) of the first five SVs' total norms. The structure of the SV in Fig. 6a implies that the absolute majority of the forecast errors can come from errors near the hurricane in the IC. The SV from the VR experiment (Fig. 6b) managed to more closely capture the fact that both the hurricane itself and the environment signals will have significant impacts on the forecast errors, as validated by the results shown in Fig. 11.

b. *Hurricane Joaquin*

Hurricane Joaquin was a major hurricane that caused significant damage in the Caribbean countries. The storm was known for its sudden shifts during its life span, casting considerable uncertainties into forecasting its future. Figure 12a shows the track and intensity evolution from its genesis on 25 September 2015. Starting from the south of Bermuda as a tropical depression, the storm gradually accumulated strength and made its first sudden southwest turn as a tropical storm toward the Bahamas, during which process Joaquin rapidly intensified to a category 4 hurricane. The storm made its second surprising turn northeastward and slightly weakened to category 3 before reintensifying to category 4 shortly afterward. The time analyzed is chosen at 0600 UTC 2 October 2015, during its second sharp turn, as marked by the cross in Fig. 12a. The spatial distributions of the geopotential and wind vector fields at 500 hPa from ERA5 are given in Fig. 12b, which will serve as the ICs for the MPAS-SW model.

Similar to Hurricane Sandy's case, the leading SVs with a 48 OTI at the analysis time under both UR and VR meshes are calculated and shown in Fig. 13. The first SV under UR mesh is predominantly sensitive to only regions near the hurricane center at the analysis time. In contrast, the leading SV from the VR experiment has significant sensitivities to areas both near

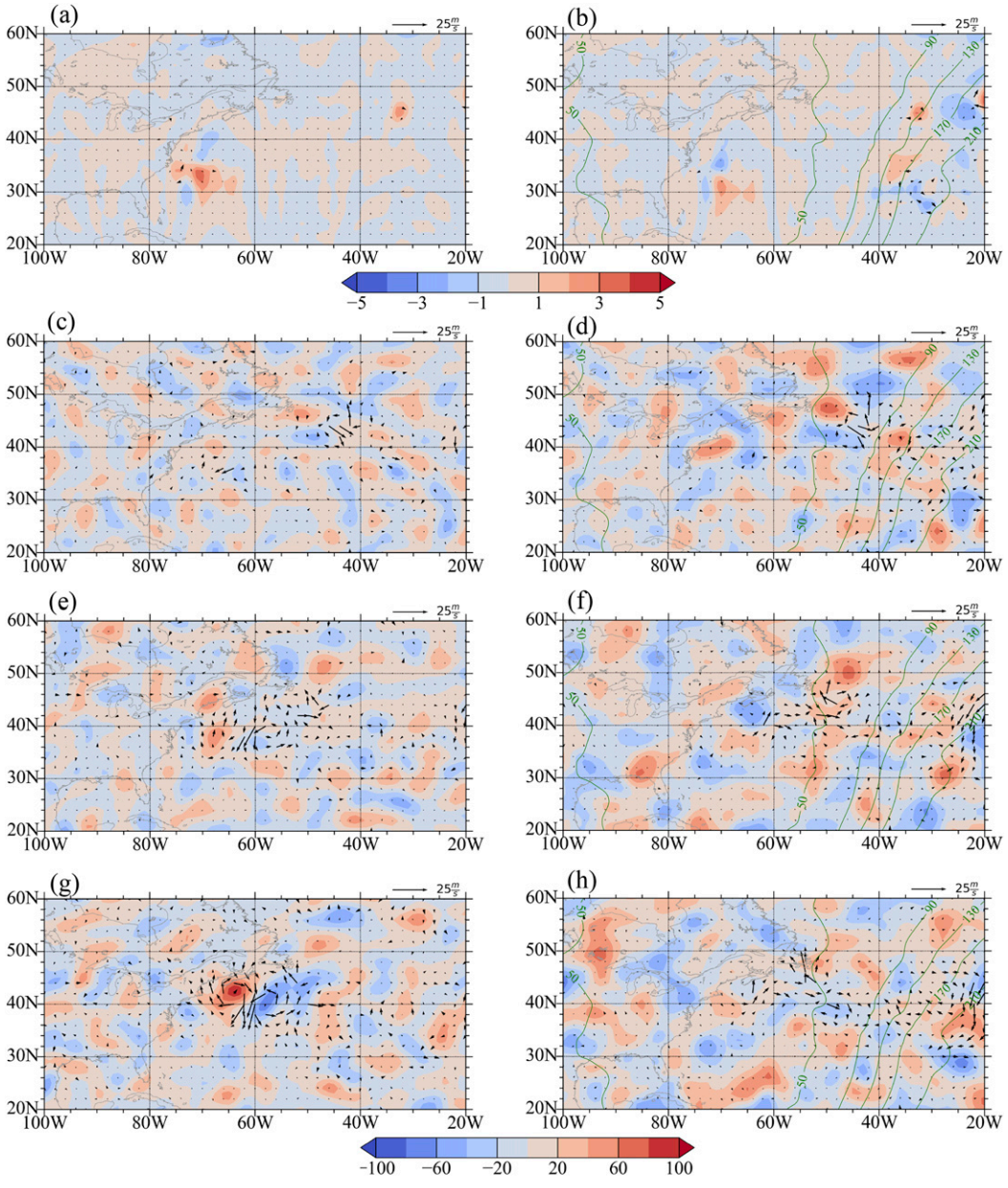

FIG. 11. The differences of the height (shaded) and wind vectors in nonlinear forward MPAS-SW simulations (left) between the UR and HR and (right) between the VR and HR in the (a),(b) 0-, (c),(d) 15-, (e),(f) 24-, and (g),(h) 30-h forecasts.

the hurricane center and far away, mostly downstream of the hurricane track, implying potential impacts on the hurricane evolution by the environmental flows in those areas. Five-day forecasts are also made with the nonlinear MPAS-SW model under UR and VR meshes with ICs shown in Fig. 12b. Figure 14 shows the predicted height and wind vector fields after 30, 48, 72, and 114 h, with the locations from the best track indicated by the green curves. In the UR experiment forecast, the cyclone in both the 30- and 48-h forecast progressed following the best track only with significantly weakened intensities. In the 72-h forecast, the storm drifted offtrack eastward and split into two parts with even weaker winds, which completely disappeared in the 114-h forecasts. Whereas in the VR experiment, throughout the 5-day forecast, the storm not only progressed closely following the best track but also maintained its intensity as in the real world with cyclonic signatures shown in Fig. 14.

6. Summary and conclusions

With rapidly growing computational power, a sophisticated atmospheric model such as the MPAS-Atmosphere is allowed

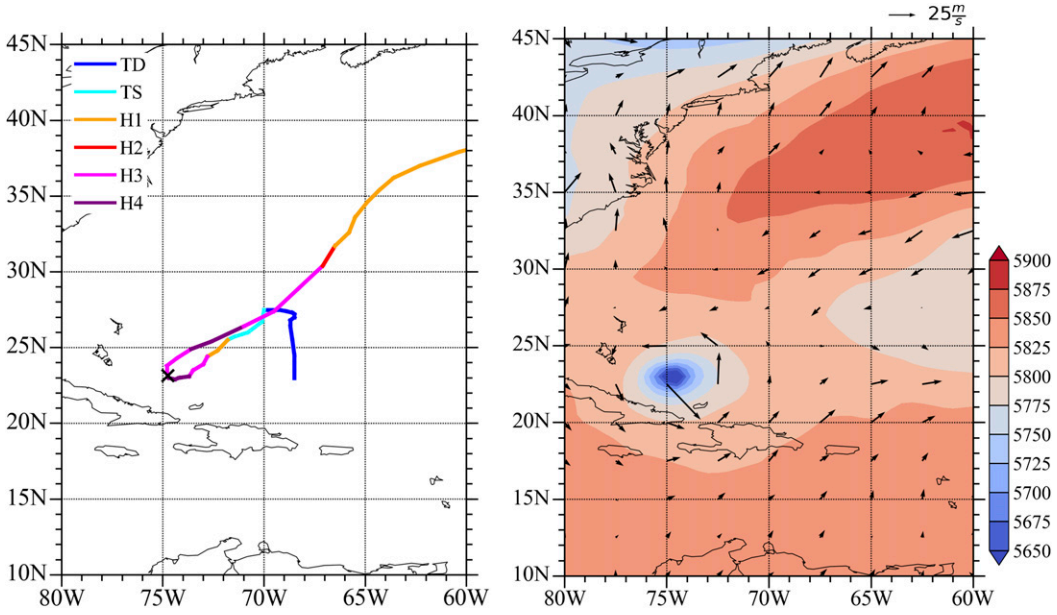

FIG. 12. (a) The track of Hurricane Joaquin from 25 Sep to 5 Oct 2015 from best track records. The colors of the curve represent the intensity of the hurricane following the Saffir–Simpson scale. The black cross marks the location of Hurricane Joaquin at 0600 UTC 2 Oct 2015. (b) The fields of height and wind vectors at 500 hPa at 0600 UTC 2 Oct 2015.

to simulate the atmospheric motions more and more closely with a greater and greater number of degrees of freedom (Skamarock et al. 2012). At the same time, simple dynamical models are still remarkably useful in resembling certain aspects of the atmosphere. The shallow water model is such an example. In this research, the global shallow water model under the irregular spherical centroidal Voronoi tessellations of the MPAS framework was adopted. The tangent linear and adjoint models of the MPAS-SW are first developed manually line by line. Necessary correctness verification procedures were conducted to ensure that the TL/AD models of the MPAS-SW are developed correctly. Among many of their potential usefulnesses, such as sensitivity analysis and variational data assimilation, the TL/AD models of MPAS-SW are readily applicable in calculating the desired number of singular vectors. The case of Hurricane Sandy was selected to compare the predictabilities under the mesh with a uniform resolution of 120 km (40 962 cells), the mesh of variable resolutions from 48 to 240 km (30 210 cells), and the mesh of uniform high resolution of 30 km (655 362 cells). Taking the height and wind vectors at 500 hPa from the ERA5 dataset as ICs, it proves that the MPAS-SW TL model is able to well approximate the evolutions of perturbations added into the ICs.

With a total perturbation energy norm, the leading SVs of a 48-h optimization time for the MPAS-SW TL model are calculated with the Lanczos algorithm, an iterative method to solve large-scale eigenvalue/eigenvector problems allowing the matrix to be implicitly expressed. In this study, the leading SVs of 48-h optimization time in cases of both Hurricanes Sandy and Joaquin are calculated. The results suggest that the leading SV accounts for the absolutely greatest amplification of errors in the ICs during this 48-h forecast period. The structures of the first SV from the experiments with the variable-resolution and the high-resolution meshes well agree with the study of

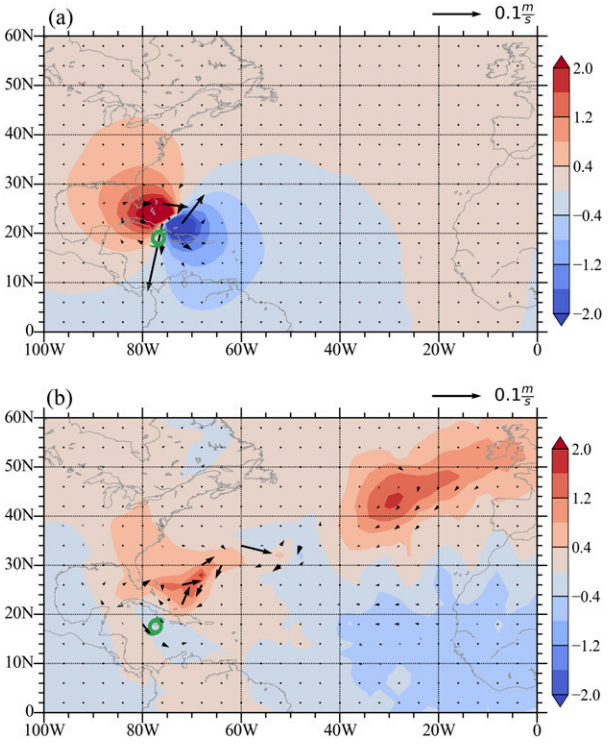

FIG. 13. The distributions of h (shaded) and $\mathbf{u}$ (vectors) in the leading singular vector with a 48-h optimization time interval from (a) UR and (b) VR experiments in the case of Hurricane Joaquin at 0600 UTC 2 Oct 2015.

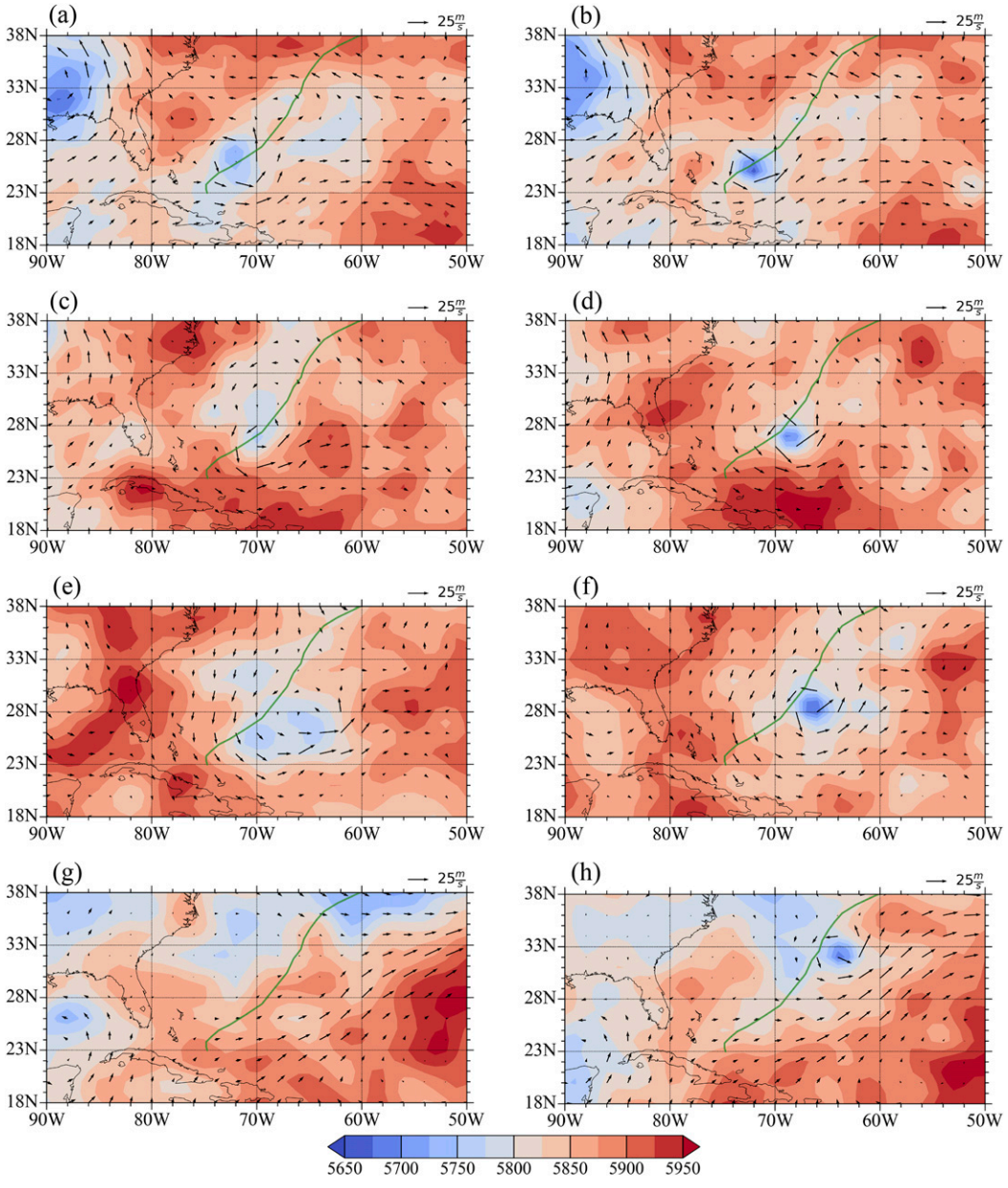

FIG. 14. Spatial distributions of the height (shaded) and wind vectors under (left) UR and (right) VR in the (a),(b) 30-, (c),(d) 48-, (e),(f) 72-, and (g),(h) 12-h forecasts starting from 0600 UTC 2 Oct 2015. The green curve indicates the best track records for Hurricane Joaquin.

Kim and Jung (2009) that the forecast are significantly sensitive to the environmental flows at the time of hurricane's recurvature. The SV results with the uniform-resolution mesh at the same analysis time was not able to capture such a feature, implying weaker predictability over the same region yet more expensive computation than the VR. The forecasts with nonlinear MPAS-SW model further verified that both the VR and HR, to some extent, were able to reproduce the sharp recurvature of Hurricane Sandy and maintain its dominant strength while interacting with a polar cyclone in the environment. In contrast, Hurricane Sandy was erroneously entrained into the environmental polar cyclone in the simulations with the UR mesh. The comparisons of the nonlinear MPAS-SW forecasts from both UR and VR experiments to those from the HR further verifies that the features both near and far away from the hurricane captured in the leading SV in VR experiment play significant roles in the forecast results.

Similar results with VR mesh in Hurricane Joaquin at the time of its recurvature were also obtained that the leading singular vector successfully captured the environmental factor, while the results with UR mesh failed to do so.

The track forecast of Hurricane Joaquin with the VR mesh was also significantly more realistic than that with the UR mesh. It should be pointed out that all the experiments in this study are in the context of shallow water dynamics, i.e., single layer with no physics. Thus, future efforts will extend this study to the more sophisticated MPAS-Atmosphere model to analyze the predictabilities under the multiresolution simulation frameworks.

Acknowledgments. The author thanks NCAR for releasing the MPAS shallow water model for public access. The author is grateful to Drs. Xiaolei Zou and William C. Skamarock for their inspirational discussions and for the anonymous reviewers' comments that helped to improve this study. The data for producing the figures are available at http://www.xiaoxutian.com/products.

REFERENCES

Borges, M. D., and D. L. Hartmann, 1992: Barotropic instability and optimal perturbations of observed nonzonal flows. *J. Atmos. Sci.*, **49**, 335–354, https://doi.org/10.1175/1520-0469(1992)049<0335:BIAOPO>2.0.CO;2.

Buizza, R., 1994: Sensitivity of optimal unstable structures. *Quart. J. Roy. Meteor. Soc.*, **120**, 429–451, https://doi.org/10.1002/qj.49712051609.

——, and T. N. Palmer, 1995: The singular-vector structure of the atmospheric global circulation. *J. Atmos. Sci.*, **52**, 1434–1456, https://doi.org/10.1175/1520-0469(1995)052<1434:TSVSOT>2.0.CO;2.

Demaria, M., S. D. Aberson, K. V. Ooyama, and S. J. Lord, 1992: A nested spectral model for hurricane track forecasting. *Mon. Wea. Rev.*, **120**, 1628–1643, https://doi.org/10.1175/1520-0493(1992)120<1628:ANSMFH>2.0.CO;2.

Errico, R. M., 1997: What is an adjoint model? *Bull. Amer. Meteor. Soc.*, **78**, 2577–2592, https://doi.org/10.1175/1520-0477(1997)078<2577:WIAAM>2.0.CO;2.

——, and T. Vukicevic, 1992: Sensitivity analysis using an adjoint of the PSU-NCAR mesoscale model. *Mon. Wea. Rev.*, **120**, 1644–1660, https://doi.org/10.1175/1520-0493(1992)120<1644:SAUAAO>2.0.CO;2.

Farrell, B. F., 1989: Optimal excitation of baroclinic waves. *J. Atmos. Sci.*, **46**, 1193–1206, https://doi.org/10.1175/1520-0469(1989)046<1193:OEOBW>2.0.CO;2.

——, and A. M. Moore, 1992: An adjoint method for obtaining the most rapidly growing perturbation to oceanic flows. *J. Phys. Oceanogr.*, **22**, 338–349, https://doi.org/10.1175/1520-0485(1992)022<0338:AAMFOT>2.0.CO;2.

Hagos, S., R. Leung, S. A. Rauscher, and T. Ringler, 2013: Error characteristics of two grid refinement approaches in aquaplanet simulations: MPAS-A and WRF. *Mon. Wea. Rev.*, **141**, 3022–3036, https://doi.org/10.1175/MWR-D-12-00338.1.

Holton, J. R., 1973: An introduction to dynamic meteorology. *Amer. J. Phys.*, **41**, 752–754, https://doi.org/10.1119/1.1987371.

Juckes, M., 1989: A shallow water model of the winter stratosphere. *J. Atmos. Sci.*, **46**, 2934–2956, https://doi.org/10.1175/1520-0469(1989)046<2934:ASWMOT>2.0.CO;2.

Kent, T., O. Bokhove, and S. Tobias, 2017: Dynamics of an idealized fluid model for investigating convective-scale data assimilation. *Tellus*, **69A**, 1369332, https://doi.org/10.1080/16000870.2017.1369332.

Kim, H. M., and B.-J. Jung, 2009: Singular vector structure and evolution of a recurving tropical cyclone. *Mon. Wea. Rev.*, **137**, 505–524, https://doi.org/10.1175/2008MWR2643.1.

Lacarra, J.-F., and O. Talagrand, 1988: Short-range evolution of small perturbations in a barotropic model. *Tellus*, **40A**, 81–95, https://doi.org/10.3402/tellusa.v40i2.11784.

Lindskog, M., N. Gustafsson, and K. S. Mogensen, 2006: Representation of background error standard deviations in a limited area model data assimilation system. *Tellus*, **58A**, 430–444, https://doi.org/10.1111/j.1600-0870.2006.00190.x.

Lorenz, E. N., 1965: A study of the predictability of a 28-variable atmospheric model. *Tellus*, **17**, 321–333, https://doi.org/10.3402/tellusa.v17i3.9076.

——, 1975: Climatic predictability. *The Physical Basis of Climate and Climate Modelling*, 132–136.

Michaelis, A. C., G. M. Lackmann, and W. A. Robinson, 2019: Evaluation of a unique approach to high-resolution climate modeling using the Model for Prediction Across Scales–Atmosphere (MPAS-A) version 5.1. *Geosci. Model Dev.*, **12**, 3725–3743, https://doi.org/10.5194/gmd-12-3725-2019.

Molteni, F., R. Buizza, T. N. Palmer, and T. Petroliagis, 1996: The ECMWF Ensemble Prediction System: Methodology and validation. *Quart. J. Roy. Meteor. Soc.*, **122**, 73–119, https://doi.org/10.1002/qj.49712252905.

Mureau, R., F. Molteni, and T. N. Palmer, 1993: Ensemble prediction using dynamically conditioned perturbations. *Quart. J. Roy. Meteor. Soc.*, **119**, 299–323, https://doi.org/10.1002/qj.49711951005.

Palmer, T. N., R. Buizza, F. Molteni, Y. Q. Chen, and S. Corti, 1944: Singular vectors and the predictability of weather and climate. *Philos. Trans. Roy.*, **348A**, 459–475, https://doi.org/10.1098/rsta.1994.0105.

Park, S.-H., W. C. Skamarock, J. B. Klemp, L. D. Fowler, and M. G. Duda, 2013: Evaluation of global atmospheric solvers using extensions of the Jablonowski and Williamson baroclinic wave test case. *Mon. Wea. Rev.*, **141**, 3116–3129, https://doi.org/10.1175/MWR-D-12-00096.1.

Rauscher, S. A., and T. D. Ringler, 2014: Impact of variable-resolution meshes on midlatitude baroclinic eddies using CAM-MPAS-A. *Mon. Wea. Rev.*, **142**, 4256–4268, https://doi.org/10.1175/MWR-D-13-00366.1.

Ringler, T., L. Ju, and M. Gunzburger, 2008: A multiresolution method for climate system modeling: Application of spherical centroidal Voronoi tessellations. *Ocean Dyn.*, **58**, 475–498, https://doi.org/10.1007/s10236-008-0157-2.

——, J. Thuburn, J. B. Klemp, and W. C. Skamarock, 2010: A unified approach to energy conservation and potential vorticity dynamics for arbitrarily-structured C-grids. *J. Comput. Phys.*, **229**, 3065–3090, https://doi.org/10.1016/j.jcp.2009.12.007.

Satoh, M., T. Matsuno, H. Tomita, H. Miura, T. Nasuno, and S.-i. Iga, 2008: Nonhydrostatic icosahedral atmospheric model (NICAM) for global cloud resolving simulations. *J. Comput. Phys.*, **227**, 3486–3514, https://doi.org/10.1016/j.jcp.2007.02.006.

Skamarock, W. C., J. B. Klemp, M. G. Duda, L. D. Fowler, S.-H. Park, and T. D. Ringler, 2012: A multiscale nonhydrostatic atmospheric model using centroidal Voronoi tessellations and C-grid staggering. *Mon. Wea. Rev.*, **140**, 3090–3105, https://doi.org/10.1175/MWR-D-11-00215.1.

Strang, G., and L. B. Freund, 1986: *Introduction to Applied Mathematics*. Wellesley Cambridge Press, 758 pp.

Thuburn, J., T. D. Ringler, W. C. Skamarock, and J. B. Klemp, 2009: Numerical representation of geostrophic modes on arbitrarily

structured C-grids. *J. Comput. Phys.*, **228**, 8321–8335, https://doi.org/10.1016/j.jcp.2009.08.006.

Tian, X., 2021: Evolutions of errors in the global multiresolution Model for Prediction Across Scales: Shallow Water (MPAS-SW). *Quart. J. Roy. Meteor. Soc.*, **147**, 382–391, https://doi.org/10.1002/qj.3923.

——, and X. Zou, 2016: ATMS- and AMSU-A-derived hurricane warm core structures using a modified retrieval algorithm. *J. Geophys. Res. Atmos.*, **121**, 12 630–12 646, https://doi.org/10.1002/2016JD025042.

——, and ——, 2020: Development of the tangent linear and adjoint models of the MPAS-Atmosphere dynamic core and applications in adjoint relative sensitivity studies. *Tellus*, **72A**, 1–17, https://doi.org/10.1080/16000870.2020.1814602.

Yeh, K.-S., J. Côté, S. Gravel, A. Méthot, A. Patoine, M. Roch, and A. Staniforth, 2002: The CMC–MRB Global Environmental Multiscale (GEM) model. Part III: Nonhydrostatic formulation. *Mon. Wea. Rev.*, **130**, 339–356, https://doi.org/10.1175/1520-0493(2002)130<0339:TCMGEM>2.0.CO;2.

Zou, X., F. Vandenberghe, M. Pondeca, and Y.-H. Kuo, 1997: Introduction to adjoint techniques and the MM5 adjoint modeling system. NCAR Tech. Note NCAR/TN-435+STR, 121 pp., https://doi.org/10.5065/D6F18WNM.